OPEN ACCESS
IOP Publishing
Nanotechnology
Nanotechnology **36** (2025) 235701 (10pp)
https://doi.org/10.1088/1361-6528/add89a

Characterization and discrimination of periodic nanostructures with scanning-free GEXRF

Nils Wauschkuhn[1], Yves Kayser[1,5], Jonas Baumann[2,6], Johannes Degenhardt[3], Thomas Siefke[4,7], Vinh-Binh Truong[1], Victor Soltwisch[1], Burkhard Beckhoff[1] and Philipp Hönicke[1,8,*]

[1] Physikalisch-Technische Bundesanstalt, Abbestr. 2-12, 10587 Berlin, Germany
[2] Technische Universität Berlin, Hardenbergstr. 36, 10623 Berlin, Germany
[3] Physikalisch-Technische Bundesanstalt, Bundesallee 100, 38116 Braunschweig, Germany
[4] Friedrich Schiller University Jena, Albert-Einstein-Str. 15, 07745 Jena, Germany
[5] Max Planck Institute for Chemical Energy Conversion, Stiftstr. 34-36, 45470 Mülheim an der Ruhr, Germany
[6] Bruker Nano GmbH, Am Studio 2D, 12489 Berlin, Germany
[7] Fraunhofer Institute for Applied Optics and Precision Engineering IOF, Albert-Einstein-Str. 7, 07745 Jena, Germany
[8] Helmholtz-Zentrum Berlin, Hahn-Meitner-Platz 1, 14109 Berlin, Germany

E-mail: philipp.hoenicke@ptb.de

Received 28 November 2024, revised 9 May 2025
Accepted for publication 14 May 2025
Published 22 May 2025

Abstract

As nanostructures in the semiconductor industry become smaller and more complex, non-destructive characterization methods capable of measuring buried domains become crucial. Grazing emission x-ray fluorescence (GEXRF) spectroscopy is a measurement technique capable of resolving nanometer-sized features of buried nanostructures while providing information about the sample's elemental distribution. In this work, a study was conducted to realistically assess the uncertainties of this method, considering correlations between geometric parameters. Furthermore, we showed strategies to effectively reduce the measurement time in GEXRF experiments by applying state-of-the-art single photon evaluation and machine learning denoising techniques for two-dimensional detectors. The study was performed on two different sample positions on a HfO_2/TiO_2 nanograting, where the GEXRF method was able to resolve geometric differences between them. Based on a finite element method model of the nanograting, the expected fluorescence intensities can be simulated, from which the nanostructure's geometry can be reconstructed. The reconstructed geometric shapes show good

---

[*] Author to whom any correspondence should be addressed.

agreement with atomic force microscope and transmission electron microscope measurements, highlighting the method's capability for investigating samples within the nanometer regime.

Keywords: GEXRF, FEM, periodic nanostructures, buried nanostructure characterization, nanoscale metrology

1. Introduction

The downsizing of transistors and the increasing complexity of modern transistor technologies have raised the demand for new methods for process control. This has affected technologies such as fin field effect transistor [1], Nanosheet [2], Forksheet [3], Complementary field effect transistor [4], and gate-all-around-nanowire field effect transistor [5]. Furthermore, emerging topics such as metamaterials [6], nanostructure arrays for photovoltaics [7, 8], optical devices [9], and nanostructures for geometry-induced doping [10–12] also require adequate characterization methods. Therefore, measurement technologies that can resolve features at the nanometer scale, especially non-destructive methods that can also resolve subsurface parts of the nanostructures, are important. With scanning electron microscopy (SEM), transmission electron microscopy (TEM), and atomic force microscopy (AFM), only local information of a few periods of a periodic pattern can be obtained. While AFM and SEM can not directly resolve buried domains of the nanostructure, TEM requires a destructive sample treatment in the form of a cross sectioning. Moreover, grazing incidence small-angle x-ray scattering and grazing incidence x-ray fluorescence (GIXRF) yield inherently averaged [13], representative information derived from the irradiated part of a periodic sample. However, due to the large irradiated surface, which quickly reaches over several millimeters in grazing incidence techniques, these methods are not applicable to the typical test structure pad sizes in the semiconductor industry.

A method without these disadvantages is the scanning-free grazing emission x-ray fluorescence (GEXRF) technique, which addresses these limitations, enabling the investigation of surface and subsurface features in periodic nanostructures while retaining the inherent averaging capability of GIXRF [14] to deliver representative information. Here the sample is irradiated by a tiny x-ray beam at a large incident angle, and the created x-ray fluorescence radiation is detected under small exit angles with respect to the sample surface [15]. With this method, element-sensitive and dimensional information can be assessed from the interference patterns of the various x-ray fluorescence signals in a non-destructive manner and on small test pad sizes. The scanning-free GEXRF method can be applied to periodic nanostructures [15] as well as to nanoparticles [16]. With the principle of microscopic reversibility [14], the application experience of GIXRF, such as its applicability to randomly ordered objects [13], and the consideration of roughness [17], can be transferred to GEXRF.

In 1993, Sasaki *et al* [18] first performed the scanning-free GEXRF method, using an imaging plate to characterize a monoatomic Zn layer in a film on a Au substrate. Two decades later, modern two-dimensional position-sensitive detectors were proved suitable for the scanning-free GEXRF technique [19]. In 2022, we applied the scanning-free GEXRF method to laterally periodic nanostructures to obtain their dimensional and compositional properties [15] for the first time. It was showcased that this method is applicable for homogenous nanostructure arrays with lateral sizes in the order of 100 µm × 100 µm or even below, which is compatible with typical metrology pad sizes in semiconductor manufacturing. Calculations predicted that the discrimination capability with respect to the different parameters of a nanostructure can be in the sub-nanometer range. In this study, we worked toward establishing comprehensive uncertainty budgets for the reconstructed parameters by examining the pronounced influence of the uncertainty of the exit angle coordinates on selected derived structural parameters. Furthermore, we took advantage of the etch-induced shape variations of the nanostructure dimensions across the sample to underpin the theoretically predicted discrimination capabilities with real experimental data. For the experiment in [15], a very long integration time was necessary. As this is a significant drawback of the scanning-free GEXRF technique, we aim to reduce the required integration time. We also aim to improve other aspects by integrating procedures that are more sophisticated than those in our initial research [15] throughout the whole experimental flow.

2. Experimental

2.1. Sample description

The sample considered is a nanostructure made up of grating lines with a nominal period (pitch) of 123 nm consisting of a silicon ridge with a titania (TiO_2) tip and a conformal hafnia (HfO_2) overlayer. A sketch of the cross section, including a definition of the geometric parameters used for the reconstruction, is shown in figure 1(a). During the manufacturing process, oxidation leads to the formation of a native silicon dioxide (SiO_2) layer on the silicon. The array of grating lines is nominally laterally homogeneous and has nominal dimensions of 1 mm × 15 mm. The grating lines are oriented along the larger dimension of the field (see figure 1(b)).

The sample was prepared by first cleaning a single-side polished [100] silicon wafer (Siegert, LOT314368) with an OptiWet SB30. This was followed by a 15 s Ar ion beam sputter etching to remove the native oxide from the wafer surface. After that, 50 nm of titania and 15 nm of chromium were deposited by vacuum ion beam sputtering (OIPT Ionfab 300LC). A resist mask was then fabricated by first depositing

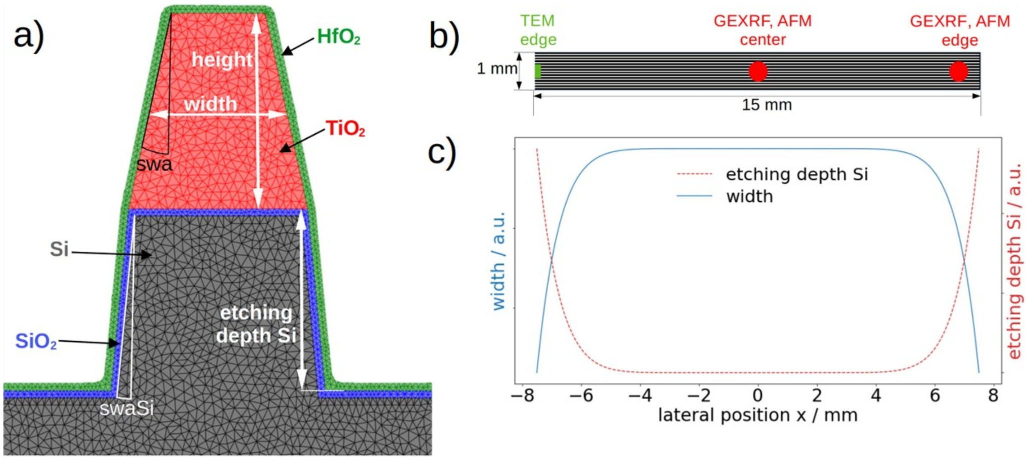

Figure 1. (a) Schematic outline of the cross section of one period of the HfO$_2$/TiO$_2$ nanograting with definitions of geometric parameters (swa = sidewall angle). (b) Dimensions, grating orientation, and an indication of the various experimental positions on the patterned area. (c) Schematic sketch of the etch-induced variations of the line width and the etching depth into the silicon for different positions on the patterned area.

HMDS from the gas phase using a Sawatec 200/300, followed by coating with OEBR-CAN038 AE 2.0CP (Tokyo Ohka Kogyo Co. LTD), exposure via electron beam lithography (Vistec 350OS, a technology working with a defocused 50 keV electron beam that homogeneously illuminates the aperture structure to be written [20]), and manual development using OPD4262. This resist mask was then transferred to the chromium layer by reactive ion etching (RIE) using a chlorine-based process, and the soft mask was then removed using an oxygen-based process (Sentech SI-591). In the next step, the hard mask was transferred to the titania layer by inductively coupled plasma etching (Sentech SI-500C) using a tetrafluoromethane-based process at −50 °C. The remaining chromium was removed by wet etching with TechniEtch Cr01. Finally, 18 cycles of hafnia were deposited by atomic layer deposition.

Due to the large open area around the field, the concentration of etch species varies on a macroscopic scale from the center to the edge of the structures. This is a well-known effect comparable to the RIE lag [21], resulting in a higher etch rate at the edges compared to the inner parts of the field. Therefore, the overall etching depth increases and the line width decreases toward the edges of the field as depicted in figure 1(c). These geometric differences were used to demonstrate the discrimination capability of the scanning-free GEXRF method: we performed two separate GEXRF experiments in the center of the field and on the edge as depicted in figure 1(b).

2.2. Scanning-free GEXRF experiments

The measurements were performed on PTB's four-crystal-monochromator beamline [22] at BESSY II under an incident angle of 45° with a monochromatic incident energy of 9.564 keV which is sufficient to excite the Hafnium L3 shell. The sample was mounted inside an ultra-high vacuum chamber with a 9-axis sample manipulator [23] to align the sample according to the incident beam and detector. We employed a scanning-free GEXRF setup using a CCD camera (SOPHIA-XO: 2048B-13.5 μm) as a detector. The grating lines were oriented perpendicularly to the plane of the CCD.

As the number of charges created by an absorbed photon in the CCD is proportional to its photon energy, the photon energy of each detected event can be retrieved from its integral deposited charge for an isolated event as described in [24, 25]. To reliably determine the integral charge deposited by an event, no overlaps with other events should persist. This requires the exposure time of the individual frames to be low enough to ensure that the probability of two photons being detected in the same or neighboring pixels is sufficiently low.

As photons can cause charge distributions spanning over more than one pixel, the charge cloud integration needs to take all CCD pixels that belong to one event into account. In our recent work [15], a histogram-based algorithm was applied, which basically considers only isolated one-pixel events and ignores multi-pixel events. In this work, an algorithm also considering the multi-pixel events was utilized. In cases where one photon causes charge depositions in more than one pixel, the intensity of all affected pixels was summed together using a clustering algorithm which is presented in detail in [26].

Dark frames (no excitation beam on the sample) were recorded to correct the electronic and readout noise pixel-wise. In both algorithms, the pixel-wise mean of the dark frames is subtracted from each frame recorded during the fluorescence measurement. In the clustering algorithm, photon events are separated from the noise by considering only pixels in which an intensity above a certain threshold is detected. The threshold was set to six times the standard deviation of the dark frame intensities measured in the same pixel. A second threshold — here three times the standard deviation of the same pixel in the dark frames — defines which intensity is required for a pixel to be considered as a neighboring pixel of a pixel fulfilling the first threshold condition or as a neighboring pixel of a cluster of pixels around a pixel fulfilling the first condition. In contrast to this, the algorithm considering

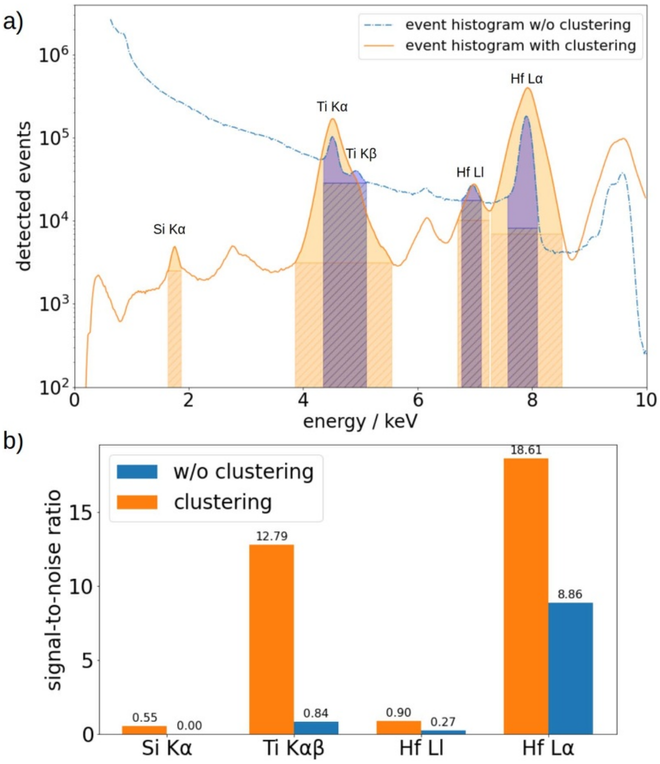

Figure 2. (a) Comparison of the spectra (recorded on the center position of the field) evaluated with the algorithm considering only one-pixel events (blue) vs. spectra evaluated with the clustering algorithm (orange), including colored areas to calculate the signal-to-noise ratio (color only: signal, shaded: noise). (b) Comparison of the signal-to-noise ratio of both algorithms for different fluorescence lines.

one-pixel events only subtracts the average of the dark frames. A comparison of the two approaches for the same set of frames (2700 frames with 15 s integration time each) from the center position of the nanograting field is shown in figure 2. For the case of the Ti Kα fluorescence line, two advantages of the clustering approach can be directly seen: the total number of detected events is larger and the contributions from the background are much lower. The signal-to-noise ratio of the clustering algorithm is much better (54.3 vs. 3.6 for the Ti Kα fluorescence line considering only the peak values). An overview of the signal-to-noise ratios of the different fluorescence lines considering the total area of the fluorescence lines is shown in figure 2(b). In both calculation variants, the signal-to-noise ratio of the clustering algorithm is about 15 times better for Ti Kα, or respectively, for the joined domain of Ti Kα and Ti Kβ. Thus, we obtain more useful events at a lower background per recorded image. The energy resolution of the total clustering spectrum (orange) is broadened by including the contribution of events consisting of many pixels. The spectrum of the two-pixel events of the clustering algorithm has a much better energy resolution, enabling the separation of Ti Kα and Ti Kβ. With the clustering algorithm, in the domains of large θ and large φ angles (see figures 3 and 4(a)), where the fluorescence intensity is theoretically nearly constant, there are on average about 2.2 times more Ti Kα events per pixel. Considering only the signal and not the noise, with the clustering algorithm there are 3.6 times more real fluorescence photon events than without clustering. As we do not consider the intensity ratios of different fluorescence lines, the different spectral efficiency is irrelevant here.

To create a GEXRF map of the fluorescence line of interest for each individual pixel, the contributions to the pixel from the identified events in the individual frames in the energy range of interest are summed together. For the reconstruction of the nanostructure, only the map of the fluorescence intensity of the Ti Kα line was considered here. To further improve the quality of the experimental Ti Kα maps, a 4×4 pixel binning and the already-trained machine learning-based noise filtering from [27] were applied. We previously performed a simple test of this denoising approach using experimental data from another experiment on the same spot of the sample by performing parameter reconstructions using all recorded frames and different fractions of the recorded frames. These reduced datasets were denoised before reconstruction and we found that the variation of the reconstructed parameters is not significantly altered by the denoising algorithm. However, if the fraction of images considered, and thus the total number of events is too low, also denoising does not help anymore. Selected results of this validation are shown later in the text in figure 8. This noise filtering is based on the assumption that the noise on a pixel is statistically independent of the noise in the neighborhood, whereas the true signal is assumed to have correlations within neighboring pixels. It reduced the variance of a region on the map with a constant theoretical XRF signal by a factor of six. A direct comparison in the same domain of the relative uncertainty resulting from the standard deviation of the Ti Kα fluorescence intensity between conditions of no clustering and no denoising versus clustering and denoising resulted in a reduction of the relative standard deviation by a factor of four, which corresponds to a reduction in the measuring period by a factor of 16.

Another crucial step in the data evaluation is the calculation of the angular θ and φ coordinates for each pixel of the CCD camera. These depend on the position of the CCD detector with respect to the illuminated spot on the sample, for example, the distance d of the pixel containing the coordinate (θ_0, φ_0), where both θ and φ are equal to zero, see figure 3.

The distance d between the sample and the CCD was determined by a relative sample rotation of $\Delta\theta$ known from the corresponding motor of the sample manipulator. Due to this rotation, the integrated x-ray fluorescence signal of the sample on the CCD was shifted. From the known relative rotation and the detector pixel size, the distance d was calculated to be 47.0(1) cm. This was performed assuming that the normal to the detector surface is contained within the sample surface at the initial position of the rotation and that the rotation axis is in the sample surface. Furthermore, the pixel where $\theta = 0^\circ$ and $\varphi = 0^\circ$ has to be determined. Since the structure can be assumed to be mirror-symmetric with respect to the vertical axis, the observed fluorescence maps are mirror-symmetric with respect to the $\varphi = 0^\circ$ axis (see figure 4(a)). Also, a tilt between the sample surface and the horizontal pixel lines can be detected and corrected in this way. Therefore,

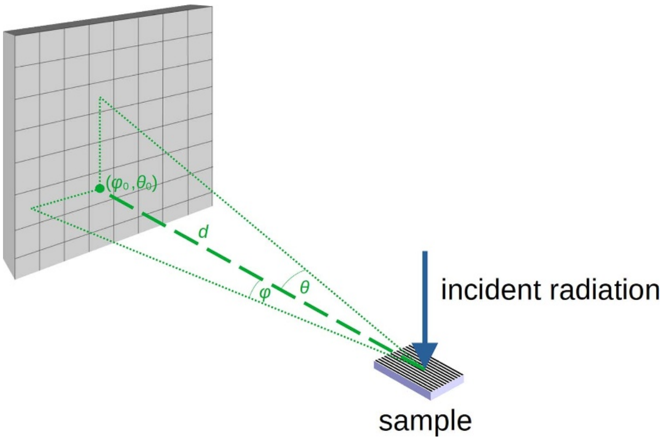

Figure 3. Setup of the scanning-free GEXRF method with geometrical definitions and the orientation of the grating lines.

φ_0 can straightforwardly be determined. The pixel axis where $\theta = 0°$ can be estimated from the onset of the fluorescence signal in the θ-direction, as nearly no signal is observed for θ angles below 0°. However, the CCD still detects events for θ below 0°, originating from scattered x-ray radiation. The diffuse limit between the domain where only noise is detected and the domain where the detected fluorescence intensity starts to emerge from the background introduces an uncertainty into the derived θ_0 coordinate which also affects the other angular coordinates as further discussed in section 3.3. The other angular coordinates were calculated geometrically from d, the (φ_0, θ_0) position, and the pixel size of 13.5 µm. With this final step of the data evaluation procedure, the GEXRF maps with angular coordinates can be generated. As an example, in figure 4(a) the GEXRF map obtained on the edge position for the Ti Kα fluorescence line is shown.

2.3. AFM measurements

To validate the GEXRF reconstruction results, AFM measurements were conducted at the same positions on the field's center and edge, where the two GEXRF experiments were performed. The AFM measurements were undertaken using a sharp tip (Nanosensors SSS) with single-point vertical probings in tapping mode, to reduce tip wear and the effect of scan artifacts [28]. The effective tip shape was calibrated on a reference sample [29] and a correction of the measured profiles was performed using the erosion approach from [30]. Despite this calibration and correction, it was not possible to eliminate all interaction effects due to the deviations between the reference sample and the nanostructure: the nanostructure exhibits a different sidewall angle and is composed of different materials than the reference sample. The slender tip could be bent toward the flanks due to attractive forces, which makes the sample appear wider.

Thus, only the total fin height but not the remaining structure geometry can be reliably determined with these vertical AFM measurements. However, the width determined through AFM follows the expected trend of being smaller at the edge position. The total fin height (height TiO_2 + etching depth Si) was determined by automatically detecting the top and bottom heights of the profiles and calculating the average height difference.

With the AFM, about 100 profiles over ten periods of the structure were acquired due to the necessity to scan, while in GEXRF, thousands of periods and a much larger part along the lines of the structure were irradiated. Consequently, the GEXRF reconstruction result represents an average over a larger area compared to the AFM result which can additionally introduce differences as the nanostructure array is not perfectly homogeneous.

3. Results and discussion

3.1. GEXRF detection of geometric variation

The first simple step was to perform a direct comparison of the fluorescence signal between the center and edge position on the sample (see figure 1(b)). The small structural differences only impose very minor differences, which are difficult to visualize in the angular maps. For this reason, the Ti Kα signal within the yellow framed boxes, seen in figure 4(a), was integrated in the φ-direction (the φ-dependence in this region is negligible). In addition, the resulting data was plotted versus the θ-coordinate in figure 4(b) for both sample positions. Two pronounced differences can easily be observed: The signal shifts to lower angles from the center to the edge as the average material density is lower due to the lower line width. Also, the oscillations at larger θ angles change their angular position and amplitude. These differences already show that the GEXRF technique is sensitive to minor structural deviations between the edge and center positions. Furthermore, these results show the importance of measuring locally isolated small domains.

3.2. Lateral GEXRF reconstruction of nanostructured surfaces

To reconstruct the geometrical parameters for both positions of the nanostructure, we employ an approach based on the finite element method (FEM) where the calculations were performed by the FEM-Maxwell solver from JCMwave [31]. Since the FEM calculations are computationally very demanding, only selected angle combinations (the red points in figure 4(a) covering the dynamic domain) were used for the reconstruction.

A sketch of the parameterized cross section of the nanostructure used for the FEM calculations is shown in figure 1(a). To find the parameters that best describe the measured fluorescence intensity distribution in a full reconstruction, the parameters are usually optimized using a Bayesian optimization approach within the JCMwave software, minimizing the residual between experimental and calculated data. But as the center position of the nanostructure was already reconstructed in our earlier work [15], and this work is focused on discriminating and reconstructing minor geometric differences, only the line width and the etch depth parameters were varied here for both positions. This was done because these parameters

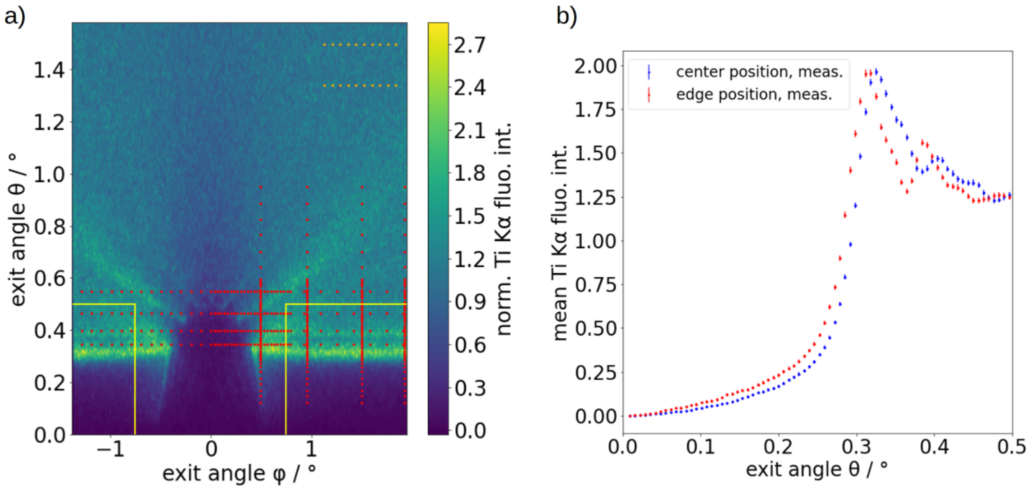

Figure 4. (a) GEXRF map of the edge position showing the selected points (red, orange) for the reconstruction (normalized to the mean value of the fluorescence intensity of the 20 points marked in orange near the top right corner) and the domains (in yellow frames) for averaging in the φ-direction. (b) Comparison edge vs. center: measured fluorescence intensity averaged in the φ-direction for all φ angles with $|\varphi| > 0.75°$ (yellow framed domains in (a)).

are expected to differ between the edge and the center position, due to the RIE lag effect in the sample's manufacturing process. The other parameters were fixed at the values determined in our earlier work as we do not expect differences between the center and the edge position in these parameters, and potential deviations are not in the scope of this work. These fixed parameters are shown in table 1. To derive the etch depth and the line width that best describe the measurement for both positions, brute-force reconstructions were performed. During this process, both parameters were varied with a step size of 0.5 nm. Moreover, the χ^2-value (sum of squared, error-weighted differences between experiment and calculation for each data point) was calculated for each combination. In figure 5, the resulting two-dimensional χ^2 distribution is shown for the edge position. From this χ^2 distribution, both the optimal etch depth and line width can be determined. Their respective confidence intervals can furthermore be estimated. The reconstructed etch depths and line widths for both edge and center measurement positions are shown in table 1, while the corresponding grating cross sections are shown in figure 6, where a comparison with the averaged AFM line profiles is depicted.

From these results, the total line height of the fin-like structure can be calculated and compared to the AFM data. The total heights for the center and the edge position are 106.8 nm and 115.3 nm, respectively, resulting in an etching depth difference between the center and the edge position of 8.5 nm, with an estimated confidence interval of ±3 nm. According to the AFM measurements, the difference in the total heights is 7.9(6) nm, which is in very good agreement with the GEXRF result. This can also be observed graphically in figure 6 where the AFM-derived line profiles are plotted with the GEXRF reconstructed cross sections for the center and edge position. The decreasing line width toward the edge, which was already observed using TEM in our earlier work [15], is also detected by GEXRF data. From the TEM, which was taken from the opposite edge and slightly further away from the center, a line width of 33 nm was derived.

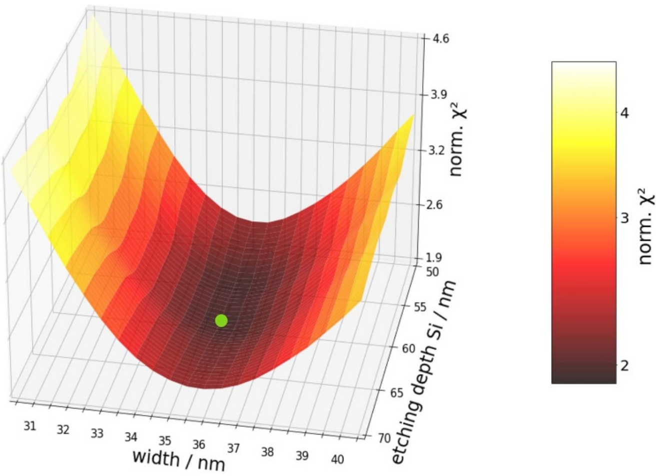

Figure 5. Three-dimensional color plot of the normalized χ^2 distribution as a function of the line width and the etch depth for the GEXRF reconstruction of the edge position. The corresponding best-fit result is indicated with a green dot.

The χ^2-distribution in figure 5 also shows the different sensitivities of the Ti Kα GEXRF data with respect to the two parameters: the sensitivity for changes in the line width is stronger since the TiO_2 is directly affected. However, changes in the etch depth do not directly affect the TiO_2. The occurring interference pattern is nevertheless still affected, resulting in less direct changes in the observed fluorescence pattern. Thus, the sensitivity for changes in the etch is less pronounced but still sufficient to reveal the differences between the edge and center. Here it should be noted that this sensitivity would be enhanced by also considering the Hf fluorescence signal as it originates from deep inside the nanograting grooves. Due to the fine angular dependence of the Hf fluorescence intensity

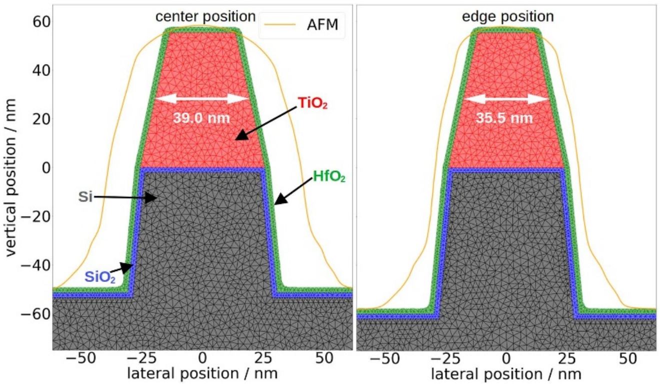

Figure 6. Comparison of the GEXRF reconstruction results for the center and edge position and corresponding AFM data (orange line).

being incompatible with the pixel binning (joining of neighboring pixels to a large pixel, as done for the Ti Kα fluorescence map), the Hf fluorescence was not used in this work.

As shown in table 1, the derived etching depths for the center position resulting from this work (51.5(30) nm) and from our initial work [15] (55.7(14) nm) differ. Also, the line width derived here is somewhat higher as compared to our earlier result. This is also depicted in figure 8, which shows the chronological order of the measurements (large dots), where clear trends are visible. Similar trends with respect to our initial experiments have been observed in a recent laboratory experiment on this nanostructure [32]. One reason for these deviations could be a possible contamination with carbonaceous residues which can grow during irradiation in a non-perfect vacuum environment from previously conducted experiments (not only GEXRF) on this sample. This may have a strong influence on the reconstruction as shown in a work by Andrle *et al* [33], and it is likely that this also has an influence here as the parameter deviations seem to increase with the number of experiments performed per spot. Furthermore, the more sophisticated frame evaluation scheme (clustering, denoising) in this work may also have an effect here because this has a strong influence, as described in section 2.2.

Table 1. Reconstruction results as determined in our earlier work [15] in comparison to the brute-force reconstruction results for the width and the etching depth of this work. The bulk densities, to which the relative densities refer, are 4.2 g cm^{-3} for TiO_2 and 9.68 g cm^{-3} for HfO_2. For the brute force reconstruction, the indicated model parameters were fixed to the earlier obtained results as they are not expected to change from center to edge positions and since the focus in this work is the resolution of minor geometric differences. From the results, a total fin height (height TiO_2 + etching depth) can be calculated and compared to the AFM results. In addition, the difference between the center and edge position as found with the GEXRF and AFM methods is shown.

parameter	center [15] (conf. int.—see text)	center, this work (conf. int.—see text)	edge, this work (conf. int.—see text)
height TiO_2 (nm)	55.3(5)	fixed at 55.3	
thickness HfO_2 (nm)	2.30(8)	fixed at 2.30	
sidewall angle (swa) (°)	12.4(3)	fixed at 12.4	
swa Si (°)	5.6(3)	fixed at 5.6	
relative density TiO_2	0.88	fixed at 0.88	
relative density HfO_2	0.84	fixed at 0.84	
etching depth Si (nm)	55.7(14)	51.5(30)	60.0(30)
width (nm)	37.7(3)	39.0(10)	35.5(10)
total fin height GEXRF (nm)	111	106.8	115.3
total fin height AFM (nm)	112 (AFM results from [15])	108.1(6)	116.0(6)
difference total fin height center vs. edge GEXRF (nm)	—	8.5(30)	
difference total fin height center vs. edge AFM (nm)	—	7.9(6)	

3.3. *Toward a comprehensive uncertainty analysis*

To reliably interpret the reconstruction results, knowing their respective uncertainties is essential. However, due to the method's complexity, an accurate error propagation would be very difficult to obtain. In our earlier work, we derived confidence intervals for each parameter from the employed Bayesian optimizer reconstruction as shown in table 1. In this work, we found that the conversion of the pixel coordinates to exit angles has a major influence on the reconstruction and is, therefore, a major source of error that was not considered in the previous work. The conversion depends on the distance between the detector surface and the illuminated beam spot on the sample, as well as the pixel position at which both θ and φ equal zero. Both of these values can only be determined with limited precision, which translates into an uncertainty of each angular coordinate. As the distance between the detector surface and the beam spot is rather large (47 cm), its relative uncertainty is small compared to the uncertainty of the $\theta = 0°$ position, which was estimated from the onset of the fluorescence signal in the θ-direction. For this procedure, based on the diffuse transition between the fluorescence signal and the background, we estimated an uncertainty of 0.01° for the emission angle offset θ_0. For φ, the assumption of symmetry of the sample and therefore of the recorded fluorescence map results in a drastically lower and thus negligible uncertainty.

To study the influence of the uncertainty of the θ-coordinates on the reconstruction results of line width and etch depth, we performed reconstructions of the datasets applying the Bayesian optimizer. These reconstructions include the width, the etching depth, and θ_0. From this reconstruction,

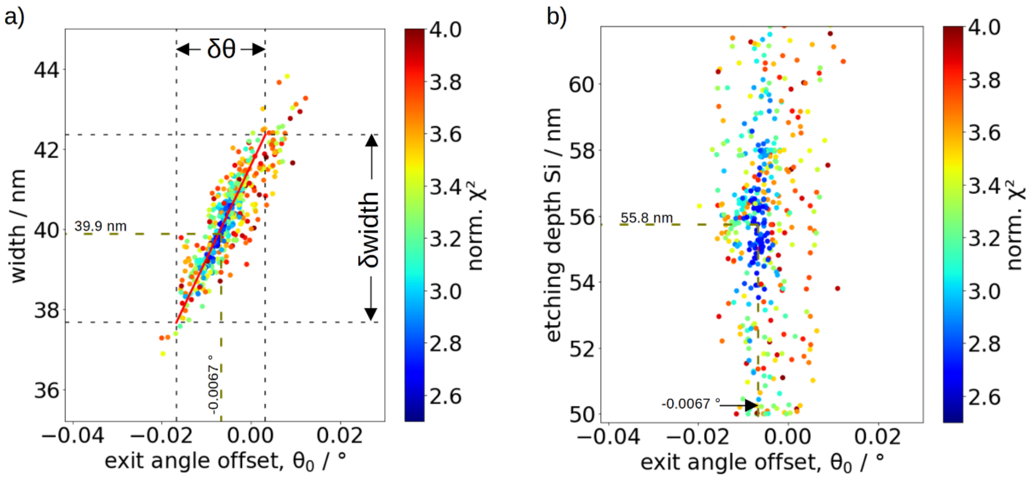

Figure 7. (a) Correlation between the θ-offset and the width parameter derived from a reconstruction of the experimental data of the center position of the field. The color coding of the dots represents the corresponding overall agreement between model and experimental data. It can clearly be seen that, depending on the picked θ-offset, a slightly different width is derived. Using the uncertainty estimate for the θ-coordinates and linear regression of the data points (red line) allows us to estimate the uncertainty of the derived width parameter. (b) The same type of plot for the etching depth parameter. No significant correlation can be found here.

one can analyze the correlations between θ_0 and the width, as well as the etching depth parameters, by plotting the respective χ^2-values as a function of the θ-offset and the width or etching depth, respectively. This is depicted in figure 7. A clear correlation for the width parameter can be observed here, whereas the etching depth is not affected by the angular offset.

Even though it should be noted that the underlying reconstruction optimization was not yet fully converged, the data still allows for a more comprehensive assessment of the uncertainty propagation with respect to the derived geometrical parameters. Employing the estimated uncertainty for the θ-coordinates of $0.01°$, one can define a confidence interval (vertical dashed lines in figure 7(a)) around the reconstructed θ-offset of $-0.0067°$. A linear regression of the points with a normalized χ^2-value of 3.25 and below allows us to determine the slope of the line plotted in red, which represents the change of the width parameter per changing θ-offset. From the intersections of this line with the estimated uncertainty of the θ-offset, we were able to derive the corresponding uncertainty of the width parameter to be 2.5 nm. As shown in 7(b), the symmetry axis in the χ^2-distribution between the etching depth and θ_0 is parallel to the coordinate axis. Consequently, the uncertainty of θ_0 does not contribute to the uncertainty of the etching depth.

As this uncertainty estimate is much larger than the derived confidence intervals in table 1, it seems to be a more realistic estimate for the full uncertainty of the derived parameters (also depicted in figure 8), as it takes all influencing experimental and methodological uncertainty contributors into account. It also demonstrates how a supposedly simple geometric conversion from pixel to angular coordinates can turn out to be a bottleneck for the achievable reconstruction uncertainties. The improvement of our strategy to measure the corresponding relative positions in the experimental setup will be part of future work.

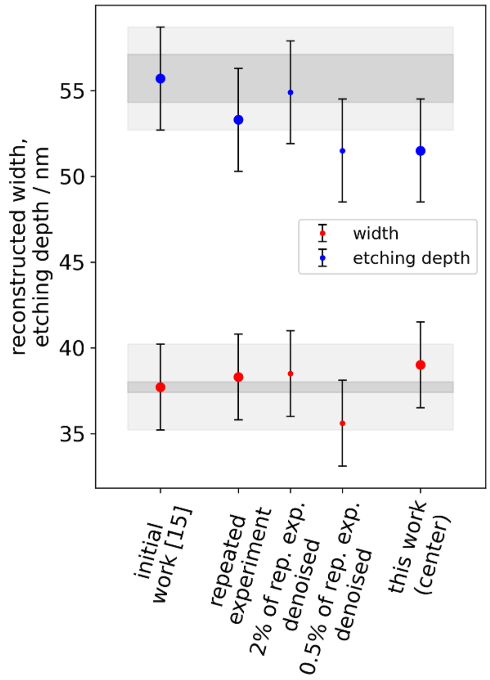

Figure 8. Overview of the different reconstruction results for width and etching depth as found in our earlier work [15], results from a repetition experiment, which was used to test the denoising filter, and the results of this work. In addition, the reconstruction results of the fractionated and denoised datasets (see text) are shown. The gray shaded areas depict the determined uncertainty estimates (light gray, see text) and the confidence intervals from [15] and table 1 (dark gray), respectively.

4. Conclusion and perspectives

In this work, a further step toward comprehensive uncertainty budgets for the reconstructed parameters is shown by analyzing the influence of uncertainties associated with the conversion from pixel to angular coordinates on the determined line width of nanostructures. In addition, we showed several improvements made to reduce the required integration time for the scanning-free GEXRF-based characterization of nanostructures as compared to our initial work [15]. By applying a clustering algorithm to derive more useful events from the recorded CCD frames and a noise reduction algorithm, which together reduced the relative standard deviation by a factor of four (corresponding to a reduction of the measuring time by a factor of 16), it was possible to reconstruct minor geometric differences: we experimentally showed that we can easily distinguish the slight modifications of the nanostructure parameters present on the employed sample using the GEXRF technique. Also, the reconstruction of the experimental data allows us to derive the different dimensions induced by etch artifacts which agree well with complementary AFM data. Notwithstanding the aforementioned new developments and progress, as well as the potential for acceleration through the utilization of much faster CMOS-based cameras instead of CCDs [32, 34], the scanning-free GEXRF-based characterization of nanostructures remains a relatively slow technique. In addition, the demonstrated influence of uncertainties related to the angular coordinates on crucial reconstructed parameters shows the necessity for identifying and incorporating all pertinent correlations within the uncertainty analysis. Furthermore, it shows the requirement for further development to make scanning-free GEXRF a useful technique for such metrology applications. One potential solution could be introducing an additional radiation source for calibration purposes, positioned in opposition to the camera [35]. The reconstruction quality could be further enhanced by incorporating data from a reference-free quantification as the efficiency of the CCD is unknown, in contrast to the efficiency of a solid drift detector employed in reference-free GIXRF [33]. In such a reference-free quantitative scanning-free GEXRF measurement, where the solid drift detector measures the absolute fluorescence intensity per incident photon during the GEXRF measurement, the loss of information due to the unknown efficiency of the CCD (due to which the normalizing on the 20 points marked in orange in figure 4 is necessary) would be compensated, although this requires reliable knowledge of the fundamental parameters of the corresponding elements.

Data availability statement

The data cannot be made publicly available upon publication because they are not available in a format that is sufficiently accessible or reusable by other researchers. The data that support the findings of this study are available upon reasonable request from the authors.

Acknowledgments

This project has received funding from the ECSEL Joint Undertaking (JU) IT2 under Grant Agreement No. 875999. The JU receives support from the European Union's Horizon 2020 research and innovation program and the Netherlands, Belgium, Germany, France, Austria, Hungary, the United Kingdom, Romania and Israel. In addition, parts of this work were carried out under the 14ACMOS (Grant Agreement Number 101096772) project, which is supported by Chips Joint Undertaking and its members, including the top-up funding of Belgium and the Netherlands.

ORCID iDs

Nils Wauschkuhn https://orcid.org/0000-0001-6187-3786
Yves Kayser https://orcid.org/0000-0002-0301-2918
Jonas Baumann https://orcid.org/0000-0002-1085-9527
Johannes Degenhardt https://orcid.org/0000-0001-5508-5556
Thomas Siefke https://orcid.org/0000-0001-6876-4080
Victor Soltwisch https://orcid.org/0000-0001-8469-8589
Philipp Hönicke https://orcid.org/0000-0002-0712-903X

References

[1] Jurczak M, Collaert N, Veloso A, Hoffmann T and Biesemans S 2009 Review of FINFET technology *2009 IEEE Int. SOI Conf.* pp 1–4
[2] Coleman J N *et al* 2011 Two-dimensional nanosheets produced by liquid exfoliation of layered materials *Science* **331** 568–71
[3] Weckx P *et al* 2019 Novel forksheet device architecture as ultimate logic scaling device towards 2nm *2019 IEEE Int. Electron Devices Meeting (IEDM)* p 36.5.1–4
[4] Ryckaert J *et al* 2018 The Complementary FET (CFET) for CMOS scaling beyond N3 *2018 IEEE Symp. on VLSI Technology* pp 141–2
[5] Nagy D, Indalecio G, GarcíA-Loureiro A J, Elmessary M A, Kalna K and Seoane N 2018 FinFET versus gate-all-around nanowire FET: performance, scaling and variability *IEEE J. Electron Devices Soc.* **6** 332–40
[6] Smalley J S T *et al* 2017 Luminescent hyperbolic metasurfaces *Nat. Commun.* **9** 8
[7] Wang W and Qi L 2019 Light management with patterned micro- and nanostructure arrays for photocatalysis, photovoltaics and optoelectronic and optical devices *Adv. Funct. Mater.* **29** 1807275
[8] LaMountain T, Lenferink E J, Chen Y-J, Stanev T K and Stern N P 2018 Environmental engineering of transition metal dichalcogenide optoelectronics *Front. Phys.* **13** 138114
[9] Gholinezhad Shafagh S, Kaatuzian H and Danaie M 2025 Design and analysis of optical devices with ultra-high quality factor based on a plasmonic photonic hybrid structure *Eng. Res. Express* **7** 015356
[10] Tavkhelidze A, Jangidze L, Skhiladze G, Sikharulidze S, Dzneladze K, Kvesitadze R and Bibilashvili A 2024 Nanograting p-n junctions with enhanced charge confinement *Nanomaterials* **14** 1889
[11] Tavkhelidze A 2014 Geometry-induced electron doping in periodic semiconductor nanostructures *Physica E* **60** 4–10
[12] Tavkhelidze A 2009 Large enhancement of the thermoelectric figure of merit in a ridged quantum well *Nanotechnology* **20** 405401
[13] Dialameh M *et al* 2018 Development and synchrotron-based characterization of Al and Cr nanostructures as potential calibration samples for 3D analytical techniques *Phys. Status Solidi a* **215** 1700866

[14] Becker R S, Golovchenko J A and Patel J R 1983 x-ray evanescent-wave absorption and emission *Phys. Rev. Lett.* **50** 153–6
[15] Hönicke P *et al* 2022 Simultaneous dimensional and analytical characterization of ordered nanostructures *Small* **18** 2105776
[16] Kayser Y, Sà J and Szlachetko J 2015 Nanoparticle characterization by means of scanning free grazing emission x-ray fluorescence *Nanoscale* **7** 9320–30
[17] Salami Z, Herrero A F, Andrle A, Hönicke P and Soltwisch V 2021 Identifying the type of line edge roughness using grazing-incidence x-ray fluorescence *Proc. SPIE* **11783** 28–35
[18] Sasaki Y C, Suzuki Y, Tomioka Y and Fukuhara A 1993 Observation of an interference effect for fluorescent x rays *Phys. Rev. B* **48** 7724–6
[19] Kayser Y, Szlachetko J and Sà J 2013 Scanning-free grazing emission x-ray fluorescence by means of an angular dispersive arrangement with a two-dimensional position-sensitive area detector *Rev. Sci. Instrum.* **84** 123102
[20] Hädrich M, Siefke T, Banasch M and Zeitner U D 2022 Optical metasurfaces made by cell projection lithography *PhotonicsViews* **19** 28–31
[21] Jansen H, de Boer M, Wiegerink R, Tas N, Smulders E, Neagu C and Elwenspoek M 1997 BSM 7: RIE lag in high aspect ratio trench etching of silicon *Microelectron. Eng.* **35** 45–50
[22] Krumrey M 1998 Design of a four-crystal monochromator beamline for radiometry at BESSY II *J. Synchrotron Rad.* **5** 6–9
[23] Lubeck J, Beckhoff B, Fliegauf R, Holfelder I, Hönicke P, Müller M, Pollakowski B, Reinhardt F and Weser J 2013 A novel instrument for quantitative nanoanalytics involving complementary x-ray methodologies *Rev. Sci. Instrum.* **84** 045106
[24] Szlachetko J, Dousse J-C, Hoszowska J, Berset M, Cao W, Szlachetko M and Kavčič M 2007 Relative detection efficiency of back- and front-illuminated charge-coupled device cameras for x-rays between 1 keV and 18 keV *Rev. Sci. Instrum.* **78** 093102
[25] Zhao W and Sakurai K 2017 CCD camera as feasible large-area-size x-ray detector for x-ray fluorescence spectroscopy and imaging *Rev. Sci. Instrum.* **88** 063703
[26] Baumann J, Gnewkow R, Staeck S, Szwedowski-Rammert V, Schlesiger C, Mantouvalou I and Kanngießer B 2018 Photon event evaluation for conventional pixelated detectors in energy-dispersive x-ray applications *J. Anal. At. Spectrom.* **33** 2043–52
[27] Krull A, Buchholz T O and Jug F 2019 Noise2void - learning denoising from single noisy images *Proc. IEEE/CVF Conf. on Computer Vision and Pattern Recognition* pp 2124–32
[28] Dai G, Häßler-Grohne W, Hüser D, Wolff H, Danzebrink H-U, Koenders L and Bosse H 2011 Development of a 3D-AFM for true 3D measurements of nanostructures *Meas. Sci. Technol.* **22** 094009
[29] Dai G, Zhu F, Heidelmann M, Fritz G, Bayer T, Kalt S and Fluegge J 2015 Development and characterisation of a new line width reference material *Meas. Sci. Technol.* **26** 115006
[30] Bukharaev A, Berdunov N, Ovchinnikov D and Salikhov K 1998 Three-dimensional probe and surface reconstruction for atomic force microscopy using a deconvolution algorithm *Scanning Microsc.* **12** 225–34
[31] Pomplun J, Burger S, Zschiedrich L and Schmidt F 2007 Adaptive finite element method for simulation of optical nano structures *Phys. Status Solidi b* **244** 3419–34
[32] Staeck S, Baumann J, Hönicke P, Wauschkuhn N, Spikermann F, Grötzsch D, Stiel H and Kanngießer B 2025 Investigation of Ti nanostructures via laboratory scanning-free GEXRF *Nanoscale* **17** 3411–20
[33] Andrle A, Hönicke P, Gwalt G, Schneider P-I, Kayser Y, Siewert F and Soltwisch V 2021 Shape- and element-sensitive reconstruction of periodic nanostructures with grazing incidence x-ray fluorescence analysis and machine learning *Nanomaterials* **11** 1647
[34] Staeck S *et al* 2022 Scan-free GEXRF in the soft x-ray range for the investigation of structured nanosamples *Nanomaterials* **12** 3766
[35] Szwedowski V, Baumann J, Mantouvalou I, Bauer L, Malzer W and Kanngießer B 2017 Scan-free grazing emission XRF measurements in the laboratory using a CCD *Phys. Status Solidi c* **14** 1700158